Creating binary Cu–Bi compounds via high-pressure synthesis: A combined experimental and theoretical study

Samantha M. Clarke,[1†] Maximilian Amsler,[2†] James P. S. Walsh,[1] Tony Yu,[3] Yanbin Wang,[3] Steven D. Jacobsen,[4] Christopher Wolverton,[2*] Danna E. Freedman[1*]

[1]Department of Chemistry, Northwestern University, Evanston, Illinois 60208, USA

[2]Department of Materials Science and Engineering, Northwestern University, Evanston, Illinois 60202, USA

[3]GeoSoilEnviroCARS, Center for Advanced Radiation Sources, The University of Chicago, Chicago, Illinois 60637, USA

[4]Department of Earth and Planetary Sciences, Northwestern University, Evanston, Illinois 60208, USA

Supporting Information Placeholder

ABSTRACT: Exploration beyond the known phase space of thermodynamically stable compounds, into the realm of metastable materials, is a frontier of materials chemistry. High pressure provides a powerful vector by which to explore this uncharted phase space, and can allow us to discover complex new structures and bonding in the solid state. We harnessed this approach for the Cu–Bi system, where the realization of new phases offers potential for exotic properties such as superconductivity. This potential is due to the presence of bismuth, which by virtue of its status as the heaviest element stable to radioactive decay forms a critical component in emergent materials such as superconductors and topological insulators. To fully investigate and understand the Cu–Bi system, we welded theoretical predictions with experiment to probe the Cu–Bi system under high pressures. By employing the powerful approach of *in situ* diffraction in a diamond anvil cell (DAC), we identified and subsequently isolated the second binary intermetallic in the Cu–Bi system, CuBi, formed by high-pressure and high-temperature (high-*PT*) reaction of the elements. Detailed comparisons between the NiAs structure type and the two high-pressure Cu–Bi phases, $Cu_{11}Bi_7$ and CuBi, reveal the preference for elemental segregation within the structure, and highlight the unique channels and layers formed by ordered Cu vacancies. Electron localization function calculations account for the presence of these "voids" as a manifestation of the lone pair orientation on the Bi atoms. Density functional theory (DFT) calculations enabled us to calculate a complementary pressure versus temperature phase diagram, which correctly predicts that CuBi is stabilized at lower pressures than $Cu_{11}Bi_7$. Our study demonstrates the power of joint experimental–computational work in simultaneously synthesizing and predicting the presence of new high-pressure intermetallic phases. The existence of multiple high-pressure-stabilized phases in the Cu–Bi binary system, which can be readily identified with *in situ* techniques, offers promise for other binary systems in which no ambient pressure phases are known to exist.

INTRODUCTION

In the quest for new metastable materials with exotic properties, high-pressure and high-temperature (high-*PT*) synthesis offers tremendous promise. In particular, the emerging technique of *in situ* monitoring of high-pressure intermetallic syntheses using diamond anvil cells (DACs) now makes it particularly convenient to perform these experiments. Metastable compounds accessed by this unconventional route exhibit unrivaled structural complexity, unique bonding, and exotic properties. Indeed, the compounds LaBi[1] and $FeBi_2$,[2,3] which were both accessed through high-pressure synthesis, exhibit pressure-induced superconductivity and the first Fe–Bi bond in the solid state, respectively. Rational, hypothesis-driven exploration within high-pressure phase space offers a route toward uncovering interesting and potentially unprecedented physical phenomena. Significant improvements made recently upon structure prediction and modeling of the effect of pressure on the enthalpy landscape and the formation of new materials enables guided exploration within the high-pressure realm. Through interfacing *in situ* high-*PT* synthesis with phase stability calculations we can expedite the discovery of new materials.

We selected the copper–bismuth binary system for exploration due to the propensity of bismuth to create emergent materials, both in its elemental form and as a component in binary intermetallic compounds. Elemental bismuth is remarkable for a variety of reasons, not least its anomalous electronic properties.[4,5,6] Emblematic of bismuth's unusual properties is the recent unexpected discovery of bulk superconductivity in pure elemental bismuth, which defies the conventional Bardeen-Cooper-Schrieffer theory model used for all other elemental superconductors.[7] The promise of bismuth binaries is significant, and during the 1960's, prominent researchers even pursued high-*PT* synthesis to isolate novel transition metal–bismuth binary compounds.[8] During that time, numerous phases were detected, but few were fully characterized due to poor yields and high structural complexity. Indeed, most of these phases were not even identified by stoichiometry. Decades later, returning to this phase space offers the potential to discover new phases, some

of which may be the same phases that previous researchers detected, but were unable to isolate.

Bismuth is unusually well-suited to high-pressure synthesis. While bismuth is highly unreactive under ambient pressures,[9-12]—to the extent it is commonly referred to as an "inert flux"—once under pressure, bismuth displays a complex energy landscape with a plethora of high-pressure polymorphs,[13-18] each exhibiting different bonding properties and structural motifs. This ability to form bonds of varying orders and geometries makes high-pressure synthesis an attractive technique for the isolation of binary intermetallic compounds.

Inspired by the prospect of isolating novel metastable compounds from high-*PT* reactions, we began an exploration of the Cu–Bi binary system. In a recent paper, we reported the first structurally characterized intermetallic compound in the Cu–Bi system, $Cu_{11}Bi_7$, synthesized by high-*PT* methods and shown to be superconducting below 1.36 K.[19] Herein, we report a combined high-pressure synthetic and theoretical exploration. By combining *in situ* diffraction experiments with phase stability calculations we probe the vast phase space of the Cu–Bi system, and subsequently isolate a new phase, the second binary intermetallic in the Cu–Bi system, CuBi. Electron localization function calculations of CuBi and $Cu_{11}Bi_7$ highlight the stereochemical activity of the lone pair on the Bi atoms, and shed light on the presence of layers and channels in these compounds. The discovery of a second superconducting Cu–Bi system at high pressures highlights the potential for the uncharted high-pressure phase space in other systems.

RESULTS AND DISCUSSION

Exploration of the copper–bismuth system. We targeted the synthesis of novel copper–bismuth binaries between 0–10 GPa due to the wealth of elemental high-pressure bismuth polymorphs that exist over this pressure range. We hypothesized that borders between the high-pressure elemental phases of bismuth would be fertile sites for the formation of new binary compounds. In order to gain insight into this system, we performed small-scale high-pressure reactions of elemental copper and bismuth in a diamond anvil cell (DAC). Using variable-temperature *in situ* synchrotron-based powder X-ray diffraction (PXRD) experiments performed at multiple pressures, we can begin to map out the experimental high-pressure phase diagram for the Cu–Bi system. In addition, such experiments can provide unique insight into formation dynamics and can facilitate the optimization of materials synthesis. In these experiments, small amounts of elemental Cu and Bi are placed in the DAC and compressed to the desired pressure (Figure SX). MgO is used as a thermal insulator between the sample and the diamond anvils and also assists in transmitting the pressure evenly throughout the cell. Further, the well-defined equation of state of MgO allows for the precise determination of pressure for each reaction. After achieving the desired pressure, we heated the elemental mixture using a microfocused infrared laser (fwhm = 40–80 μm) and we continuously monitored the reaction using *in situ* PXRD (λ = 0.406626 Å) at beamline 16-ID-B, HPCAT, Advanced Photon Source (APS).[20] Figure 1 highlights the results of the *in situ* PXRD experiments performed at multiple pressures.

The *PT* stability of the five elemental polymorphs of Bi are shown in the temperature versus pressure phase diagram for elemental Bi (Figure 1a).18 There are no known high-pressure Cu polymorphs, and Cu melts at or above 1085 °C at all pressures.

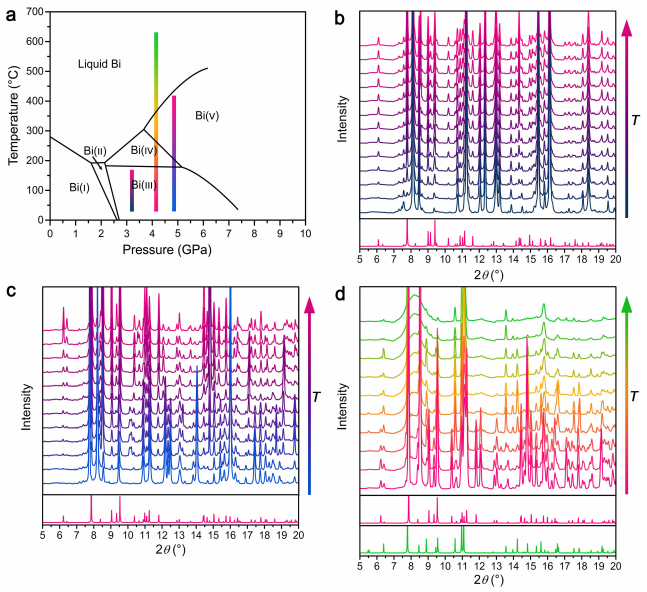

Figure 1. (a) Temperature *versus* pressure phase diagram for elemental Bi depicting the five different high-pressure polymorphs of bismuth (taken from Ref. 18). Vertical colored bars represent the approximate temperatures and pressures investigated using *in situ* X-ray diffraction in this study. Panels b–d show background-subtracted *in situ* PXRD patterns collected while heating mixtures of elemental Cu and Bi at various pressures (λ = 0.406626 Å). The simulated powder pattern of the new Cu–Bi phase formed is plotted below the experimental data (CuBi in pink and $Cu_{11}Bi_7$ in green). (b) Reaction at 3.19(1) GPa leads to the creation of CuBi as a minor phase. (c) Reaction at 4.88(1) GPa leads to peaks of the new CuBi phase increasing in intensity with increasing temperature. Peaks at ~10.1° indicate the transformation of Bi(III) into Bi(IV). The peak at 8.2° decreasing in intensity and the peak at 8.5° increasing in intensity indicate the transformation of Bi(IV) to Bi(V). (d) Heating of a pre-reacted area at 4.16(1) GPa shows the formation of $Cu_{11}Bi_7$ from CuBi and elemental Bi and Cu. Formation of this phase occurs at the melting point of elemental Bi, which is indicated by the broad intensity from 7–10°.

Therefore, elemental fcc Cu is stable over the entire region shown in Figure 1a.[21] The vertical colored bars in this figure represent the approximate pressures and temperatures investigated using the *in situ* XRD technique. The *in situ* diffraction patterns (Figures 1b–d) collected at regular intervals during heating reveal the formation of either a newly identified phase, CuBi (pink), or $Cu_{11}Bi_7$ (green) at different *PT* conditions. Figure 1b shows the reaction of the elements at ~3.19(1) GPa. In this reaction, we gradually increased the laser power, thereby heating the elemental reactants, Cu and Bi(III), from room temperature to ~150 °C. Since temperatures at this range are difficult to monitor precisely, we inferred the upper limit of temperature from the lack of Bi(IV) peaks, which are expected to grow in above 150 °C. Characteristic peaks belonging to a new phase, CuBi, begin to appear (most noticeably at 6.1, 7.8, and 10.2°), at which point we held the laser at constant power for 10 minutes. The peaks grow in intensity for approximately 4 minutes, whereupon the new phase appears to reach equilibrium with the elemental reactants. The reaction was thermally quenched by turning off the laser. Evaluation of the powder diffraction pattern acquired after cooling show the presence the new CuBi phase along

with elemental Bi(III) and Cu. This experiment illustrates that the synthetic conditions for the formation of the new CuBi phase are at relatively low pressures and temperatures (3.2 GPa, <160 °C)—far below the melting point of elemental Bi at that pressure. Therefore, the formation of CuBi progresses through a solid-state diffusion process that does not rely on the presence of elemental liquid Bi. The solid-state equilibrium reached in the synthesis suggests a competing thermodynamic stability between the reactants and product at these *PT* conditions.

To investigate the formation of new Cu–Bi compounds at slightly higher pressures, we reacted elemental copper and bismuth in a DAC at ~4.88(1) GPa (Figure c). Again, elemental reactants were heated by gradually increasing the laser power. At low power, it is apparent that CuBi is already forming based on the appearance of peaks at ~9° and 11.8°. At slightly higher power, peaks appear at ~10.1°, indicating the transformation of Bi(III) into Bi(IV). In the Bi *PT* phase diagram, this structural phase change occurs above 177 °C, allowing us to establish that the formation of CuBi begins below this temperature. As the laser power is further increased, the transformation of Bi(IV) to Bi(V) is indicated by the decrease in intensity of the peaks at ~10.1° and 8.2°, and appearance of a peak at 8.5°. This phase change occurs above 200 °C at this pressure, demonstrating how elemental structural phase changes of Bi can be used to estimate temperature during the *in situ* experiment. Throughout the entire reaction, the intensities of the CuBi peaks are increasing, indicating that higher temperatures stabilize the formation of CuBi relative to the reactants. Upon cooling, the CuBi phase remains and the Bi(V) reconverts to Bi(III).

To explore the reaction of Cu with liquid Bi at high temperatures, a third reaction was performed at a starting pressure of 4.16(1) GPa. In this reaction, a pre-reacted area containing CuBi, Cu, and Bi(III) was heated from ambient temperature to above the melting point of elemental Bi, as indicated by the broad intensity from 7–10° arising from liquid Bi (Figure 1d). This elemental phase change indicates that the reaction temperature was greater than 350 °C. For this reaction, the temperature was also measured by fitting the optical emission to the Planck radiation function and was found to reach ~800 °C. As the temperature is increased, the amount of liquid Bi increases, and CuBi gradually transforms into $Cu_{11}Bi_7$. This suggests that at 4.2 GPa and high temperatures, $Cu_{11}Bi_7$ is the more thermodynamically stable phase. As the temperature is further increased, the intensity of the peaks corresponding to $Cu_{11}Bi_7$ decrease and the intensity of the broad peak corresponding to liquid Bi increases. Upon cooling, a very small amount of $Cu_{11}Bi_7$ remains, with the majority of the product being elemental Bi(III). This experiment indicates that $Cu_{11}Bi_7$ is synthesized through a melting process—rather than through a solid-state diffusion process—at these pressures. This is corroborated by the successful LVP synthesis of $Cu_{11}Bi_7$ occurring at the melting point of Bi(V) (~530 °C) under a pressure of ~6 GPa.

From these *in situ* diffraction experiments, we can begin to construct an experimental phase diagram. From the lower temperature experiments, we know that between 3.2 and 4.8 GPa and below the melting point of elemental Bi, CuBi is the thermodynamically stable phase. By probing the temperatures above the melting point of elemental Bi at 4.2 GPa, we learned that $Cu_{11}Bi_7$ and CuBi are both stable, with $Cu_{11}Bi_7$ being the high-temperature stabilized phase, potentially formed through the melting of elemental Bi. Clearly, the use of *in situ* diffraction provides valuable insight into formation dynamics of these new intermetallic compounds, and has the immediate potential to increase the efficiency of materials discovery and optimization

Scale-up and isolation of the new binary CuBi. The complexity of the powder diffraction patterns obtained from the new CuBi phase meant that they were resistant to structural solution approaches. We therefore worked to scale up this reaction to create a sample suitable for structural analysis. A large volume press housed at the Advanced Photon Source facilitated this scale up and enabled the characterization of this new material. The binary Cu–Bi compounds were obtained in >85% yield by reaction of the elements at high pressures and temperatures using a large volume multi-anvil press. Specifically, CuBi was formed from reaction of the elements at ~4 GPa and ~250 °C for 5 minutes, and $Cu_{11}Bi_7$ is formed at ~6 GPa and ~530 °C for 1 hour.19 The samples were cooled to ambient temperature by switching off the current to the resistive heater and the samples were slowly decompressed by releasing pressure in the hydraulic pumps.

The complex high-pressure structures of these compounds are quenchable (*i.e.* they remain intact at ambient pressures), allowing for their full structural and electronic characterization under ambient conditions. Both compounds are metastable at ambient pressure and temperature, with decomposition temperatures of T_d = 158 °C and 130 °C for CuBi and $Cu_{11}Bi_7$, respectively, determined via differential scanning calorimetry (Figure SX). The higher decomposition temperature of CuBi indicates a higher ambient-pressure stability, which is expected given that it is the lower-pressure stabilized intermetallic. The obtained ambient-pressure lattice parameters for each compound reveal the density of CuBi and $Cu_{11}Bi_7$ to be 10.481 g/mol and 10.6587 g/mol, respectively. Again, the higher density in $Cu_{11}Bi_7$ is consistent with it being the phase stabilized at higher pressures.

Structure Descriptions. Due to the layered structure of CuBi, crystals of sufficient size for single crystal X-ray diffraction could not be isolated from the large volume press reaction product. Therefore, the structure was solved by Rietveld refinement of the synchrotron PXRD pattern. The pattern was indexed to the orthorhombic space group *Pmma* with unit cell parameters a = 5.18899(2) Å, b = 4.23081(2) Å, and c = 7.86634(3) Å. A search of the Inorganic Crystal Structure Database (ICSD)[22] for known structures with similar symmetry and lattice parameters yielded orthorhombic $Mn(Bi_{0.85}Sb_{0.15})$ as a close match.[23,24] We used the atomic positions from this structure as a starting point for the refinement of CuBi. The composition determined from energy-dispersive X-ray spectroscopy (EDS) is in excellent agreement with the composition determined from the crystal structure (Figure SX).

The complex, commensurately modulated structure of $Cu_{11}Bi_7$ was solved using single crystal X-ray diffraction. Details of the structure solution are explained in detail in an earlier report.19 Briefly, the compound crystallizes in a hexagonal sublattice with additional satellite reflections around the main ones. A (3 + 1)-dimensional crystallographic approach was used to solve the commensurate supercell in the superspace group $Pm(a1/2\gamma)s$ with final unit cell parameters a = 8.5907(4) Å, b = 5.2542(3) Å, c = 8.5931(5) Å, β = 120.013(2)°, and a commensurate modulation vector $q = 1/3a^* + 1/2b^* + 1/3c^*$.

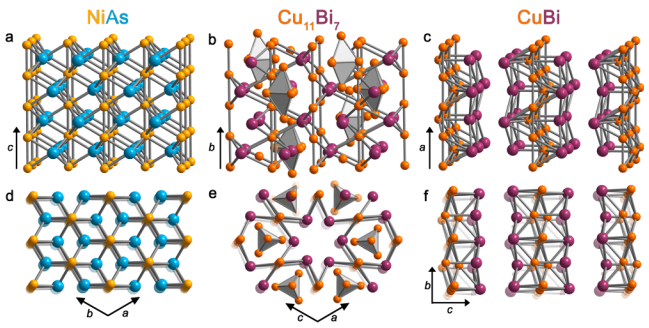

Figure 2. Comparison of the crystal structures of $Cu_{11}Bi_7$ (b, e) and CuBi (c, f) with the NiAs structure type (a, d). Yellow, blue, orange, and violet spheres represent Ni, As, Cu, and Bi, respectively. Striking differences from the NiAs structure-type include the trigonal bipyramids formed by the Cu atoms in $Cu_{11}Bi_7$ (b) and the trigonal prismatic, square face monocapped interstitial Cu atoms in CuBi (c). View along the transition-metal chain direction shows the Cu vacancies in $Cu_{11}Bi_7$ (e) and CuBi (f).

Both structures can be understood by their similarity to the canonical NiAs ($B8_1$) structure type. Figure 2 depicts the relationship of the novel Cu–Bi structures to that of NiAs. The NiAs structure type is composed of hexagonal close packed (hcp) As (or pnictogen *Pn*) atoms where the octahedral interstices are occupied by Ni (or transition metal *T*) atoms (Figure 2a and 2d).[25] The Ni–Ni (or *T*–*T*) bonding interaction along the *c*-axis forms linear Ni chains with short separations (d = 2.519 Å). The key differences between this structure type and the new Cu–Bi binary compounds arise from ordered vacancies and interstitial occupancy of the Cu atoms.

The $Cu_{11}Bi_7$ binary differs from the NiAs structure type in that an ordered vacancy of the Cu chains generates empty one-dimensional channels formed exclusively of Bi trigonal antiprisms that are face-sharing along the *b*-axis (Figure 2e and 3b). The opening of these clearly visible channels is estimated to be the distance between a Bi atom and the line formed by the other two Bi atoms belonging to the same plane, which is $d_{ave} \approx 3.34$ Å. The shortest Bi–Bi bonding interaction is along the *b*-axis between Bi atoms belonging to different planes ($d_{ave} \approx 3.44$ Å), and is much longer than what would be expected from doubling the covalent radii of Bi ($2r_{Bi}$ = 2.96 Å)[26], suggesting weak Bi–Bi interactions in this compound. Another unique feature of this compound is the presence of Cu_5 trigonal bipyramids, which alternate with Bi atoms along the *b*-axis (Figure 1b). Within the Cu_5 cluster, the Cu–Cu bond distances vary from 2.518–2.580 Å between equatorial Cu atoms to 2.609–2.687 Å between an equatorial and an apical Cu atom. The weaker bonding interaction is likely due to the higher coordination number of the apical Cu atoms (CN = 9) compared to the equatorial ones (CN = 8).[27] The Cu_5 bipyramid structure can be envisioned as capped over all faces by the Cu atoms from the Cu chains, forming a larger Cu_{11} cluster that is apical-vertex-sharing with a dicapped trigonal prismatic coordinated Bi atom along the *b*-axis (Figure 3b). This larger structure is edge sharing in the *ac*-plane to form a Cu framework (Figure 3b). There are two shortest Cu–Bi bonds; the first is between the apical Cu_5 atoms and Bi atoms composing the channel ($d_{ave} \approx 2.77$ Å) and the second is between the trigonal prismatic coordinated Bi atom and the coordinating Cu atoms ($d_{ave} \approx 2.79$ Å). The rest of the Cu–Bi interactions are greater than the sum of the covalent radii ($r_{Cu} + r_{Bi}$ = 2.81 Å).26 The well separated Cu framework and Bi channels represent elemental segregation within the intermetallic compound, which reflects the preference for full segregation of the elements at standard conditions (Figure 2b).

Similar to $Cu_{11}Bi_7$, CuBi departs from the NiAs structure type and instead crystallizes in the Co_2InTb structure type.[28] This structure can be generated from the NiAs structure type by an ordered vacancy of Cu chains, which gives rise to a unique layered structure (Figure 1c and 1f). An additional Cu2 site within the lattice displaces the Bi atoms to form an overall puckered two-dimensional triangular net of Cu atoms. Within this net, there are two short Cu–Cu bonds between the Cu1 and Cu2 (2.5632(2) Å), a slightly longer bond between two Cu1 atoms (2.5945(0) Å), and one long bond between Cu2 atoms (2.8949(6) Å). The Bi atoms are severely distorted from the hexagonal close packing arrangement found in the NiAs structure type and form a puckered two-dimensional rhombus network. Bond distances between the Bi atoms are 3.3801 Å, which again are significantly longer than doubling the covalent radii of Bi (2.96 Å).26 The two-dimensional Bi network is attached to both sides of the Cu net, creating a bonding interaction between the Cu and Bi atoms. Cu1 and Cu2 each have a bonding interaction with Bi1 at a distance of 2.8200(5) Å and 2.8227(2) Å, respectively, which agrees well with the sum of the covalent radii (2.81 Å).26 On the other hand, there are two Bi2–Cu1 interactions; one is very short (2.6816(8) Å) and the other is very long (2.9469(4) Å). The very short bond indicates strong Cu–Bi interactions between these two atoms. Similar to the structure of $Cu_{11}Bi_7$, the presence of two-dimensional elemental sheets stacking in a repeating sequence of Bi–Cu–Bi along the *c*-axis reflects the preference for segregation of the elements at standard conditions (Figure 3a).

Of the known binary first row transition-metal–bismuth compounds, MnBi and NiBi crystallize in the NiAs structure type. The low-temperature (LT) phase of MnBi has the ideal NiAs crystal structure; however, a high-temperature phase stable above 340 °C exhibits a disordered NiAs structure type whose exact structure is still debated, but likely contains Mn atoms in interstitial positions.[29] Similarly, NiBi has recently been found to have Ni atoms in interstitial positions and partial Ni vacancies in the transition metal chains.[30,31] From this trend, the interstitial Cu atoms are not unprecedented; however, ordered Cu vacancies that create channels and layers in the novel Cu–Bi intermetallics are certainly unusual. Future work will focus on revealing a correlation between the electronic structure and the absence or presence of electron-lined voids in these materials, and will potentially lead to the targeted design of such layered intermetallic compounds.

Electron Localization Function calculations. The distinguishing feature of the Cu–Bi binary intermetallic compounds is that of channels and layers formed by bismuth atoms (Figure 3). We attribute these features to nonbonding electrons, or stereochemically active lone pairs, on the Bi atom. The stereochemical activity of lone pairs is frequently observed in compounds containing cationic Bi^{3+}.[32] However, the stereochemical activity of Bi atoms in intermetallic compounds is less common. One example is $RhBi_4$, which features highly localized lone pairs that are located on the Bi atoms and directed into the space between Rh–Bi polyhedral nets.[33] The authors commented that the existence of regions with very different valence electron localization creates a microscopic anisotropy. They propose that this anisotropy influences the electro-kinetical properties and may correlate with the superconductivity of the material. In the ternary Ti_4TBi_2 (*T* = Cr, Mn, Fe, Co, Ni) com-

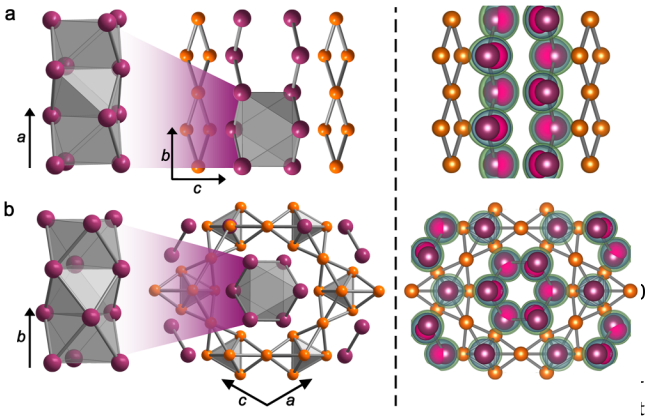

Figure 3. The left panel highlights the pillars formed by the Bi atoms and the crystal structures of CuBi (a) and $Cu_{11}Bi_7$ (b), with orange and purple spheres representing Cu and Bi, respectively. Only Cu–Cu and Bi–Bi bonds are drawn to highlight the elemental segregation within the structure. The right panel shows isosurfaces of the electron localization function (ELF), highlighting the voids formed by the bismuth atoms in each structure. ELF isosurface values of 0.7, 0.8, and 0.9 are shown in green, blue, and pink, respectively. The highly localized ELF isosurfaces indicate lone pairs on the Bi atoms that point toward the center of the voids.

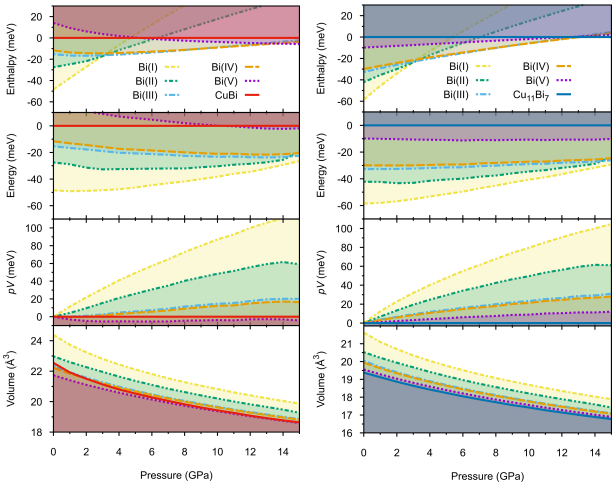

Figure 4. DFT enthalpies $H = E + PV$ of CuBi and $Cu_{11}Bi_7$ in panel a and b, respectively, at 0 K as a function of pressure with respect to elemental decomposition into Cu and the various polymorphs of bismuth. The top panel shows the enthalpy differences, whereas the second panel contains the static energies. The pressure term PV is plotted in the third panel, and the bottom panel shows the atomic volumes.

pounds, "empty channels" formed by slightly distorted edge-sharing bismuth tetrahedra highlight the presence of a lone pair.[34] Beyond these examples, very few studies of the lone pairs in intermetallic Bi compounds have been reported, potentially due to the paucity of such materials. Therefore, CuBi and $Cu_{11}Bi_7$ add to the unique category of bismuth-based intermetallic compounds with stereochemically active lone pairs.

To gain further insight into the unique structural features formed by the Bi atoms, electron localization function (ELF) calculations of $Cu_{11}Bi_7$ and CuBi were performed. High ELF values correspond to regions of high electron localization, such as bonds or lone pairs. The calculated ELF values are limited to the range of 0 to 1. In the right panel of Figure 3, ELF isosurface values of 0.7, 0.8, and 0.9 are shown in green, blue, and pink, respectively.

A section of the ELF is shown in the *bc*-plane passing through the Bi atoms in CuBi, clearly showing the layered nature of this compound (Figure 3a). The lone pairs of the Bi atoms can be clearly observed between the individual layers, indicated by the pink isosurface at a value of ELF = 0.9. Similarly, a section of the ELF is shown in the *ab*-plane of $Cu_{11}Bi_7$, illustrating the presence of channels in the structure and the preference of the highly localized electrons to point toward the void (Figure 2b). The calculation of such highly localized electrons pointing toward the voids further support our assignment of stereochemically active lone pairs.

The presence of electron-lined voids in both compounds could facilitate the intercalation of electrophilic species, and could prove to be specifically useful in battery or ionic conductivity applications. The distance from the center to the vertices of the Bi trigonal antiprisms that compose the channels in $Cu_{11}Bi_7$ ranges from 2.57 Å to 2.60 Å. In CuBi, the layer is composed of severely distorted Bi trigonal antiprisms where the distance from the center of the antiprism to Bi2 is 2.29 Å and to Bi1 is 2.86 Å. While the space in both compounds seems rather narrow, there is enough room for the intercalation H^+ and Li^+, with estimated bismuth contact distances of 1.76 and 2.05 Å, respectively. Surprisingly, there could even be enough room for the intercalation of the alkali-metal cation Na^+ in $Cu_{11}Bi_7$, with an expected contact distance of 2.41 Å. These results highlight the potential future chemical utility of these high pressure solids with electron-lined voids.

Calculated Cu–Bi high-pressure phase diagram. Theoretical methods have been proven to be extremely useful in predicting novel materials at extreme pressures. The power and accuracy of structure prediction in conjunction with density functional theory calculations has been demonstrated for various materials. For example the discovery of unexpected stoichiometry in the Na-Cl system[35] and the first helium compound[36] were both initially predicted from first principles calculations. To this end, *ab initio* calculations were performed to independently investigate the theoretical stability of the new phases as a function of pressure and temperature.

MHM simulations were carried out at variable compositions to sample the enthalpy landscape at pressures of 0 and 10 GPa. At the 1:1 stoichiometry, the *Pmma* structure of CuBi was recovered as the lowest enthalpy structure, with lattice parameters of a = 5.2036 Å, b = 4.26321 Å, and c = 8.13071 Å at 0 GPa, in excellent agreement with the experimental results. To our surprise—and in contrast to the $Cu_{11}Bi_7$ phase, which only becomes enthalpically stable at pressures above approximately 12 GPa—CuBi has a positive formation enthalpy over all pressures. In fact, the pressure at which CuBi exhibits the smallest formation enthalpy (5.5 meV/atom) is about 14 GPa, a value which is significantly higher than the pressures used to experimentally synthesize CuBi of 3–5 GPa.

Elevated temperatures can promote the formation of compounds and phase transitions in two manners. On one hand, high temperature is required to overcome kinetic barriers that need to be surmounted for a phase transformation. On the other hand, it changes the thermodynamic conditions and can lead to a shift in the stability of different phases. Since the samples of CuBi and $Cu_{11}Bi_7$ had been both synthesized at elevated temperatures of

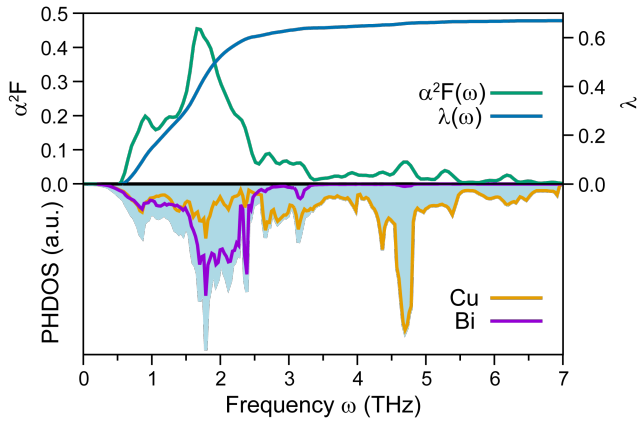

Figure 6. The electron-phonon coupling properties of CuBi at 0 GPa. The Eliashberg spectral function and the integrated coupling constant are shown in the top panel, whereas the partial PHDOS are shown in the lower panel, respectively. The shaded area indicates the total PHDOS.

above 50 °C (323 K) we decided to compute the vibrational entropy within the harmonic approximation to assess the complete Gibbs free formation energies.

The stability of the new CuBi *Pmma* phase was evaluated with respect to elemental decomposition, taking also into account the recently discovered $Cu_{11}Bi_7$ phase at high pressure. In contrast to Cu, which remains in the face centered cubic (fcc) structure, elemental bismuth undergoes a series of phase transition upon compression, which are summarized in Figure 1a and explained in the SI. Figure 5 shows the pressure–temperature phase diagram of CuBi and $Cu_{11}Bi_7$ with respect to elemental decomposition, while Figures SX and SX show the range of negative formation free energies of the two compounds separately. The free energy contributions were evaluated from the vibrational entropy computed at every pressure in steps of 1 GPa. For pure Bi, DFT is able to qualitatively reproduce the experimental phase diagram. However, the pressures and temperatures of the transition from Bi(III) to Bi(IV) and from Bi(IV) to Bi(V) are severely overestimated, a behavior which has been reported before.[37] Nevertheless, we can qualitatively deduce the main factors which stabilize CuBi and $Cu_{11}Bi_7$. The phase boundaries of both binaries with respect to elemental decomposition differ significantly from each other. For $Cu_{11}Bi_7$, the phase boundary at 0 K is 11.7 GPa and has a negative slope, extending to 7.9 GPa at 1000 K. Hence, pressure alone would suffice to render $Cu_{11}Bi_7$ thermodynamically stable, and elevated temperatures merely decrease the transition pressure. On the other hand, elevated temperatures are necessary to reach conditions where CuBi is thermodynamically stable (shown by the red region in Figure 5 and SX), where it indeed exhibits negative formation free energies. In fact, the only way to stabilize CuBi is by increasing the pressure and simultaneously using temperatures significantly above 0 K. The combined phase diagram shows that CuBi is stable at lower pressures compared to $Cu_{11}Bi_7$. However, the diagram also contains a narrow pressure-temperature region wherein both compounds simultaneously lie on the convex hull of stability. Note that liquid phases were neglected in our calculations, and that imaginary phonons emerge at conditions where Bi is experimentally reported to melt (denoted by the dashed lines).

To understand how pressure influences the stability of CuBi and $Cu_{11}Bi_7$, we plotted the various contributions to the enthalpy as a function of pressure in Figures 4a and 4b. The top panels indicate the enthalpy differences with respect to elemental decompositions against the various Bi phases and Cu. As mentioned above, there is no pressure region where the formation enthalpy of CuBi is negative in Figure 4a, although the magnitude decreases rapidly as the pressure increases. The enthalpy, $H = E + PV$, can be decomposed into the static energy, E, and the pressure term, PV, which are shown in the second and third panels, respectively. Similar to the enthalpy, the energy term is positive over the whole pressure range. The main driving force behind the stabilization of CuBi must therefore come from the pressure term. Indeed, the difference in PV is negative with respect to all elemental Bi phases except for Bi(V) at pressures above 1 GPa. This behavior can be readily explained by investigating the atomic volumes, plotted in the bottom panel. Due to the high compressibility of CuBi, its volume decreases rapidly between 0 and 8 GPa, above which it asymptotically approaches a value close to Cu + Bi(V). Combined with the high vibrational entropy term, S, arising from the weak interlayer bonds, the formation Gibbs free energy, $G = E + PV - TS$ becomes negative as temperature is increased at pressures above 7 GPa. An analogous analysis of $Cu_{11}Bi_7$ shown in Figure 4b indicates a completely different stabilization mechanism. In contrast to CuBi, the PV term is always negative at finite pressures due to the small atomic volume. Therefore, it is only a matter of increasing the pressure until PV dominates the formation enthalpy, leading to the thermodynamic stability of $Cu_{11}Bi_7$ without any need to include entropic effects.

Calculated superconducting properties. To further investigate the electronic structure of CuBi, we computed the superconducting properties at 0 GPa based on the Allan-Dynes modified McMillan's approximation of the Eliashberg equation.[38] Similar calculations for $Cu_{11}Bi_7$ were reported previously. A Coulomb pseudopotential value of $\mu^* = 0.13$ was used, which was shown to give a T_c in excellent agreement with the experimental values in $Cu_{11}Bi_7$. For CuBi, we obtain a superconducting transition temperature of $T_c = 1.7$ K. This is slightly higher than the preliminary experimental values of $T_c = 1.33$–1.40 K (Figure SX). This discrepancy in T_c of around 0.3 K lies well with the expected accuracy of DFT calculations, and can be readily corrected by using a slightly higher value of μ^*: using $\mu^* = 0.14$ lowers the T_c to 1.5 K, whereas $\mu^* = 0.15$ yields $T_c = 1.4$ K. We can therefore conclude that CuBi is a conventional superconductor with a rather moderate electron–phonon coupling constant of $\lambda = 0.67$, comparable to the value of $\lambda = 0.63$ computed for $Cu_{11}Bi_7$.

The upper panel of Figure 6 shows both the Eliashberg spectral function, $\alpha^2F(\omega)$, and the frequency-dependent coupling constant $\lambda(\omega)$. It is evident that phonons in the frequency range between 0 and 3 THz contribute primarily to the overall coupling strength. This low energy range is in fact strongly dominated by the Bi vibrations, as indicated in the lower panel of Figure 6, where the total phonon density of states (PHDOS) together with the partial, atom projected PHDOS are shown. Again, this behavior is consistent with the calculations in $Cu_{11}Bi_7$, where the Bi atoms mainly contribute to the electron–phonon coupling. Susceptibility measurements on CuBi demonstrate superconductivity at a comparable temperature to $Cu_{11}Bi_7$. We tentatively attribute the similarity in critical temperatures to the similar Bi framework found in the two compounds.

CONCLUSIONS

The foregoing results describe the efficacy of synthesis experiments performed in a DAC which allow for *in situ* powder X-ray diffraction at high-*PT* conditions. These experiments provide valuable insight into the formation dynamics of CuBi and $Cu_{11}Bi_7$ and pave the way toward efficient intermetallic materials discovery in high-pressure phase space. Through these experiments, we report the isolation and study of the heretofore-unknown intermetallic compound CuBi. Similar to the recently reported $Cu_{11}Bi_7$ compound, the structure can be described as a derivative of the NiAs structure type. Computational studies demonstrate that the stereochemically active lone pairs on the Bi atoms influence the structure of both unusual binary compounds. These lone pairs create channels and layers in $Cu_{11}Bi_7$ and CuBi, respectively. To further investigate these structure details, we analyzed the electronic structure and chemical bonding of these compounds using ELF calculations, which confirm our assignment of stereochemical active lone pairs on the Bi atoms. DFT calculations independently confirm that CuBi is the lower-pressure-stabilized phase. Further, they predict superconductivity in CuBi, similar to that found in $Cu_{11}Bi_7$. Future work will focus on stabilizing these phases using ambient-pressure synthetic techniques.

EXPERIMENTAL

Synthesis of bulk samples. Sample synthesis and characterization of $Cu_{11}Bi_7$ is described elsewhere.19 The bulk synthesis of CuBi is described below. Note, the *in situ* experiments, which also resulted in the formation of CuBi and $Cu_{11}Bi_7$ are described in a subsequent section. Metal reagents were purchased from commercial vendors and used as received. Sample synthesis proceeded by mechanical ball milling the elements to create a uniform powder, followed by high-pressure synthesis in a large volume press. In a dinitrogen atmosphere, a 50 mL agate ball-milling crucible was charged with Cu powder (5.5 mmol, 0.3496 g), Bi powder (5.5 mmol, 1.1505 g), and seven alumina balls. Ball milling was performed for 4 hours at a rate of 250 rpm using a Retsch planetary ball mill PM 100. Milling was stopped for 30 minutes every hour to allow for the dissipation of heat and to prevent cold welding. High-pressure reactions were performed using the 1000-ton multi-anvil large volume press (LVP) at 13-BM-D, GeoSoilEnviroCARS (Sector 13), Advanced Photon Source (APS), Argonne National Laboratory. The 14/8 "G2" COMPRES cell assembly used for these reactions is described in detail elsewhere.[39] We modified this reaction setup by using a boron nitride crucible as a reaction container, which is more inert to reaction with metals than the standard magnesium oxide crucible (Figure SX). The highest purity samples were obtained via the following procedure. Samples were compressed to 135 tons over 4 hours, which corresponds to a sample pressure of 4 GPa based on previously obtained calibration curves. The pressure was held for 15 minutes at ambient temperature. Samples were then heated using a resistive heater at a power output of 150 W. The thermocouple reported a temperature of 250 °C. Samples were annealed for five minutes then rapidly cooled to room temperature by turning off the heater's power supply. The pressure was released steadily over 5 hours. The resulting samples was cylindrical in shape, with a diameter of ~1.5 mm and a height of ~1.5 mm with a silver-metallic color.

Crystallographic and elemental characterization. Scanning electron microscopy (SEM) was performed on a Hitachi S-3400N-II using a 25 kV electron beam and energy-dispersive X-ray spectroscopy (EDS) for semiquantitative elemental analysis was acquired with an Oxford INCAx-act SSD. Samples were mounted on conductive carbon tape on aluminum stages. Fifteen points over a ~0.4 mm^2 area were averaged to obtain a composition of $Cu_{50.1(2)}Bi_{49.9(2)}$, which corresponds to an atomic formula of $Cu_{1.1(3)}Bi_{0.9(3)}$ when scaled to the formula unit. The samples are well sintered as shown by the secondary electron images which feature a very small amount of cracks and crevices (Figure S3). Small Cu and Bi-rich areas are seen in the SEM images.

The structure of CuBi was solved by Rietveld refinement of the synchrotron powder X-ray diffraction (PXRD) pattern from the high-resolution 11-BM diffractometer at the Advanced Photon Source, Argonne National Laboratory, with an incident wavelength of λ = 0.414203 Å. The samples were coated on the outside of a Kapton capillary using Dow Corning #4 electrical insulating grease, cooled to 100 K, and spun at ~600 rpm during collection. Powder diffraction data were analyzed by the Rietveld method using the computer program TOPAS.[40] The pattern was fit in the 2θ range of 2 to 40 and the background was fit using a Chebyshev polynomial with 30 parameters. Unreacted elemental Bi and Cu were fit along with the new phase. Stephens model line broadening was employed for each phase. The peaks corresponding to the new phase can be indexed to the orthorhombic space group *Pmma* with unit cell parameters a = 5.18898(2) Å, b = 4.23079(1) Å, and c = 7.86656(2) Å. A search of the Inorganic Crystal Structure Database (ICSD)22 listed $Mn(Bi_{0.85}Sb_{0.15})$ as having similar symmetry and lattice parameters (*Pmma*, a = 5.70 Å, b = 4.27 Å, and c = 7.40 Å).23,24 We used the atomic positions from this structure as a starting point for the refinement of CuBi. Further details are found in the SI. The synchrotron PXRD pattern indicates near complete conversion of the elements into CuBi (88.80%) with a small amount of residual elemental Cu (8.31%) and Bi (2.88%) (Figure S3).

Details of in situ experiments. All of the *in situ* laser heating and synchrotron powder X-ray diffraction (PXRD) experiments were performed at Beamline 16-ID-B, HPCAT, Advanced Photon Source (APS), Argonne National Laboratory, Illinois, USA. During the reaction experiments samples were heated using an *in situ* double-sided laser heating setup.[41] High intensity monochromatic synchrotron radiation with a fixed wavelength of 0.406626 Å was used for all diffraction experiments. Details of diamond anvil cell design can be found in the SI.

Computational methods. The Minima Hopping structure prediction method (MHM)[42,43] within the Minhocao package implements a highly reliable algorithm to identify the ground state structure of compounds solely given the chemical composition.[44-47] Within this method the low lying part of the enthalpy landscape is efficiently sampled by performing consecutive, short molecular dynamics escape steps to overcome enthalpy barriers, followed by local geometry optimizations. The Bell-Evans-Polanyi principle is exploited by aligning the initial molecular dynamics velocities along soft mode directions in order to accelerate the search.[48,49]

Energies, forces and stresses were evaluated from density functional theory (DFT) calculations within the projector augmented wave (PAW) formalism[50] was implemented in the VASP package[51-53] together with the Perdew-Burke-Ernzerhof (PBE) approximation to the exchange correlation potential.[54] A plane-wave cutoff energy of 400 eV was used with a sufficiently dense k-point mesh to ensure a convergence of the total energy to within 4 meV/atom. Both the atomic and cell parameters were simultaneously relaxed until the maximal force components were less than 4 meV/Å.

Phonon calculations were carried out with the frozen phonon approach as implemented in the PHONOPY package using sufficiently large supercells for converged thermal properties.[55] To compute the vibrational contribution to the free energy a dense mesh of 30 x 30 x 30 was used to sample the Brillouin zone. The harmonic free energy at temperature T was computed according to

$$F(T) = E + \int \frac{\hbar\omega}{2} g(\omega) d\omega + \int \hbar\omega ln\left(1 - e^{\left(-\frac{\hbar\omega}{k_b T}\right)}\right) g(\omega) d\omega$$

where E is the static energy, and $g(\omega)$ is the phonon density of states at frequency ω.

The Quantum Espresso package was used to compute the phonon-mediated superconducting properties.[56] We used ultra-soft pseudopotentials and a plane-wave cutoff energy of 40 Ry. The Allan-Dynes modified McMillan's approximation of the Eliashberg equation[57] was used to estimate the superconducting temperature:

$$T_c = \frac{\omega_{log}}{1.2} \exp\left[-\frac{1.04(1+\lambda)}{\lambda - \mu^*(1+0.62\lambda)}\right]$$

where μ^* is the Coulomb pseudopotential, lambda is the overall electron-phonon coupling strength computed from the frequency dependent Eliashberg spectral function $\alpha^2 F(\omega)$, and ω_{log} is the logarithmic average phonon frequency. A 6 x 6 x 4 q-mesh was used together with a denser 24 x 24 x 16 k-mesh for the *Pmma* structure, resulting in a well converged superconducting transition temperature T_c. A value of μ^*=0.13 was employed, which was shown to give a T_c in excellent agreement with experimental results obtained for $Cu_{11}Bi_7$.[19]

ASSOCIATED CONTENT

Supporting Information

This material is available free of charge via the Internet at http://pubs.acs.org.
Experimental details, differential scanning calorimetry, scanning electron microscopy, temperature-pressure formation free energies,
Rietveld refinement parameters.

AUTHOR INFORMATION

Corresponding Author

*Email: c-wolverton@northwestern.edu (C.M.W.)
*Email: danna.freedman@northwestern.edu (D.E.F.)

Author contributions

†These authors contributed equally.

Notes

The authors declare no competing financial interests.

ACKNOWLEDGMENT

We thank Dr. Yue Meng for experimental assistance. This experimental work is supported by DARPA (W911NF15100069) and the AFOSR (FA95501410358), and used resources of the APS (DOE: DE-AC02-06CH11357). GeoSoilEnviroCARS at the APS is supported by the NSF (EAR-1128799) and DOE (DE-FG02-94ER14466). S.M.C. acknowledges support from the NSF GRFP (DGE-1324585). M.A. and C.W. (DFT calculations) acknowledge support from the Novartis Universität Basel Excellence Scholarship for Life Sciences and the Swiss National Science Foundation (P300P2-158407), and DOE (DE-FG02-07ER46433). Computational resources from the Swiss National Supercomputing Center in Lugano (Project s700), the Extreme Science and Engineering Discovery Environment (XSEDE) (which is supported by National Science Foundation grant number OCI-1053575), the Bridges system at the Pittsburgh Supercomputing Center (PSC) (which is supported by NSF award number ACI-1445606), the Quest high performance computing facility at Northwestern University, and the National Energy Research Scientific Computing Center (DOE: DE-AC02-05CH11231), are gratefully acknowledged. This work made use of the IMSERC at Northwestern University, which has received support from the Soft and Hybrid Nanotechnology Experimental (SHyNE) Resource (NSF NNCI-1542205); the State of Illinois and International Institute for Nanotechnology (IIN).

REFERENCES

(1) Tafti, F. F.; Torikachvili, M. S.; Stillwell, R. L.; Baer, B.; Stavrou, E.; Weir, S. T.; Vohra, Y. K.; Yang, H.-Y.; McDonnell, E. F.; Kushwaha, S. K.; Gibson, Q. D.; Cava, R. J.; Jeffries, J. R. Tuning the Electronic and the Crystalline Structure of LaBi by Pressure. *Phys. Rev. B* **2017**, *95*, 014507.

(2) Walsh, J. P. S.; Clarke, S. M.; Meng, Y.; Jacobsen, S. D.; Freedman, D. E. Discovery of $FeBi_2$. *ACS Cent. Sci.* **2016**, *1*, 668–669.

(3) Amsler, M.; Naghavi, S. S.; Wolverton, C. Prediction of Superconducting Iron–Bismuth Intermetallic Compounds At High Pressure. *Chem. Sci.* **2017**, *8*, 2226–2234.

(4) Yang, F. Y.; Liu, K.; Hong, K.; Reich, D. H.; Searson, P. C.; Chien, C. L. Large Magnetoresistance of Electrodeposited Single-Crystal Bismuth Thin Films. *Science*, **1999**, *284*, 1335–1337.

(5) Tian, M.; Wang, J.; Kumar, N.; Han, T.; Kobayashi, Y.; Liu, Y.; Mallouk, T. E.; Chan, M. H. W. Observation of Superconductivity in Granular Bi Nanowires Fabricated by Electrodeposition. *Nano Lett.* **2006**, *6*, 2773–2780.

(6) Li, L.; Checkelsky, J. G.; Hor, Y. S.; Uher, C.; Hebard, A. F.; Cava, R. J.; Ong, N. P. Phase Transitions of Dirac Electrons in Bismuth. *Science*, **2008**, *321*, 547–550.

(7) Prakash, O.; Kumar, A.; Thamizhavel, A.; Ramakrishnan, S. Evidence for Bulk Superconductivity in Pure Bismuth Single Crystals At Ambient Pressure. *Science*, **2017**, *355*, 52–55.

(8) Matthias, B. T.; Jayaraman, A.; Geballe, T. H.; Andres, K.; Corenzwit, E. Many More Superconducting Bismuth Phases. *Phys. Rev. Lett.* **1966**, *17*, 640-643.

(9) Kanatzidis, M. G.; Pöttgen, R.; Jeitschko, W. The Metal Flux: A Preparative Tool for the Exploration of Intermetallic Compounds. *Angew. Chem. Int. Ed. Engl.* **2005**, *44*, 6996–7023.

(10) Thompson, C. M.; Tan, X.; Kovnir, K.; Garlea, V. O.; Gippius, A. A.; Yaroslavtsev, A. A.; Menushenkov, A. P.; Chernikov, R. V; Buttgen, N.; Kratschmer, W.; Zubavichus, Y. V; Shatruk, M. Synthesis, Structures, and Magnetic Properties of Rare-Earth Cobalt Arsenides, RCo_2As_2 (R = La, Ce, Pr, Nd). *Chem. Mater.* **2014**, *26*, 3825–3837.

(11) Phelan, W. A.; Nguyen, G. V; Wang, J. K.; McCandless, G. T.; Morosan, E.; DiTusa, J. F.; Chan, J. Y. Discovery of Spin Glass Behavior in $Ln_2Fe_4Sb_5$ (Ln = La–Nd and Sm). *Inorg. Chem.* **2012**, *51*, 11412–11421.

(12) Thompson, C. M.; Kovnir, K.; Eveland, S.; Herring, M. J.; Shatruk, M. Synthesis of $ThCrSi_2$-Type Arsenides from Bi Flux. *Chem. Commun.* **2011**, *47*, 5563–5563.

(13) Brugger, R. M.; Bennion, R. B.; Worlton, T. G. The Crystal Structure of Bismuth-II at 26 Kbar. *Phys. Lett. A* **1967**, *24*, 714–717.

(14) Chen, J. H.; Iwasaki, H.; Kikegawa, T.; Yaoita, K.; Tsuji, K. Crystal Structure of the High Pressure Phase of Bismuth BiIII. *AIP Conf. Proc.* **1994**, *309*, 421–424.

(15) Degtyareva, O.; McMahon, M. I.; Nelmes, R. J. Crystal Structure of the High Pressure Phase of Bismuth Bi-III. *Mater. Sci. Forum* **2001**, *378–381*, 469–475.

(16) Chaimayo, W.; Lundegaard, L. F.; Loa, I.; Stinton, G. W.; Lennie, A. R.; McMahon, M. I. High-Pressure, High-Temperature Single-Crystal Study of Bi-IV. *High Press. Res.* **2012**, *32*, 442–449.

(17) Schaufelberger, P.; Merx, H.; Contre, M. Structure Cristalline Du Bismuth V. *High Temp. Press.* **1973**, *5*, 221–230.

(18) Klement, W.; Jayaraman, A.; Kennedy, G. C. Phase Diagram of Arsenic, Antimony, and Bismuth at Pressures up to 70 Kbars. *Phys. Rev.* **1963**, *131*, 632–637.

(19) Clarke, S. M.; Walsh, J. P. S.; Amsler, M.; Malliakas, C. D.; Yu, T.; Goedecker, S.; Wang, Y.; Wolverton, C.; Freedman, D. E. Discovery of a superconducting Cu–Bi compound by high-pressure synthesis. *Angew. Chem. Int. Ed.* **2016**, *55*, 13446–13449.

(20) Meng, Y.; Hrubiak, R.; Rod, E.; Boehler, R.; Shen, G. New Developments in Laser-Heated Diamond Anvil Cell with in Situ Synchrotron X-Ray Diffraction at High Pressure Collaborative Access Team. *Rev. Sci. Instrum.* **2015**, *86*, 72201.

(21) Akella, J.; Kennedy, G. C. Melting of Gold, Silver, and Copper—proposal for a New High-Pressure Calibration Scale. *J. Geophys. Res.* **1971**, *76*, 4969–4977.

(22) Inorganic Crystal Structure Database (ICSD) Web, Version 3.5.0, FIZ Karlsruhe, Germany, **2017**.

(23) Göbel, H.; Wolfgang, E.; Harms, H. Properties of MnBi Compounds Partially Substituted with Cu, Zn, Ti, Sb, and Te. I. Formation of Mixed Phases and Crystal Structures. *Phys. Status Solidi* **1976**, *34*, 553–564.

(24) Cenzual, K.; Gelato, L. M.; Penzo, M.; Parthe, E.; Parthé, E. Inorganic Structure Types with Revised Space Groups. I. *Acta Crystallogr. Sect. B* **1991**, *47*, 433–439.

(25) Alsen, N. Roentgenographische Unterschungen der Kristallstrukturen von Magnetkies, Breithauptit, Pentlandit, Millerit und verwandten Verbindungen. *Geol. Foeren. Stockholm Foerh.* **1925**, *47*, 19–73.

(26) James, A. M.; Lord, M. P. *Macmillan's Chemical and Physical Data*; Macmillan Press, London, **1992**.

(27) CN computed from Cu–Cu distances below 2.66 Å and Cu–Bi distances below 2.88 Å.

(28) Kalychak, Y. M.; Zaremba, V. I.; Pecharsky, V. K. Crystal Structure of Terbium Cobalt Indium (1/2/1), $TbCo_2In$. *Z. Kristallogr.* **1993**, *205*, 333-334.

(29) Willis, B. T. M.; Rooksby, H. P. Magnetic Transitions and Structural Changes in Hexagonal Manganese Compounds. *Proc. Phys. Soc. Sect. B* **1954**, *67*, 290–296.

(30) Lidin, S.; Petricek, V.; Stenberg, L.; Furuseth, S.; Fjellvag, H.; Larsson, A.-K. The Incommensurately Modulated Structure of NiBi. *Solid State Sci.* **2000**, *2*, 353–363.

(31) Ruck, M. Die Kristallstruktur von BiNi : Eine Komplexe Ausdünnungsvariante Des $InNi_2$-Typs. *Z. Anorg. Allg. Chem* **1999**, *625*, 2050–2054.

(32) Walsh, A.; Payne, D. J.; Egdell, R. G.; Watson, G. W. Stereochemistry of Post-Transition Metal Oxides: Revision of the Classical Lone Pair Model. *Chem. Soc. Rev.* **2011**, *40*, 4455–4463.

(33) Grin, Y.; Wedig, U.; von Schnering, H. G. Hyperbolic Lone Pair Structure in $RhBi_4$. *Angew. Chemie Int. Ed.* **1995**, *34*, 1204–1206.

(34) Rytz, R.; Hoffmann, R. Chemical Bonding in the Ternary Transition Metal Bismuthides Ti_4TBi_2 with T = Cr, Mn, Fe, Co, and Ni. *Inorg. Chem.* **1999**, *38*, 1609–1617.

(35) Zhang W.; Oganov, A. R.; Goncharov, A. F.; Zhu, Q.; Boulfelfel, S. E.; Lyakhov, A. O.; Stavrou, E.; Somayazulu, M.; Prakapenka, V. B.; Konpkov, Z. Unexpected Stable Stoichiometries of Sodium Chlorides, *Science*, **2013**, 342, 1502.

(36) Dong, X; Oganov, A. R.; Goncharov, A. F.; Stavrou, E.; Lobanov, S.; Saleh, G.; Qian, G. R.; Zhu, Q.; Gatti, C.; Deringer, V. L.; Dronskowski, R.; Zhou, X. F.; Prakapenka, V. B.; Konôpková, Z.; Popov, I. A.; Boldyrev, A. I.; Wang, H. T. A Stable Compound of Helium and Sodium at High Pressure. *Nature Chemistry*, **2017**, 10.1038/nchem.2716.

(37) Häussermann, U., Söderberg, K. & Norrestam, R. Comparative Study of the High-Pressure Behavior of As, Sb, and Bi. *J. Am. Chem. Soc.* **2002**, *124*, 15359–15367.

(38) Allen, P. B. & Dynes, R. C. Transition Temperature of Strong-Coupled Superconductors Reanalyzed. *Phys. Rev. B* **1975**, *12*, 905–922.

(39) K. D. Leinenweber, J. A. Tyburczy, T. G. Sharp, E. Soignard, T. Diedrich, W. B. Petuskey, Y. Wang, J. L. Mosenfelder, *Am. Mineral.* **2012**, *97*, 353.

(40) Coelho, A. A. *TOPAS Academic: General Profile and Structure Analysis Software for Powder Diffraction Data*, Bruker AXS, Karlsruhe, Germany, **2007**.

(41) Meng, Y.; Hrubiak, R.; Rod, E.; Boehler, R.; Shen, G. New Developments in Laser-Heated Diamond Anvil Cell with *In Situ* Synchrotron X-ray Diffraction at High Pressure Collaborative Access Team. *Rev. Sci. Instrum.*, **2015**, *86*, 072201.

(42) Amsler, M; Goedecker, S. Crystal Structure Prediction Using the Minima Hopping Method, *The Journal of Chemical Physics*, **2010**, 133, 224104.

(43) Goedecker, S. Minima Hopping: An Efficient Search Method for the Global Minimum of the Potential Energy Surface of Complex Molecular Systems, *J. Chem. Phys.*, **2004**, 120, 9911.

(44) Amsler, M.; Flores-Livas, J. A.; Lehtovaara, L.; Balima, F.; Ghasemi, S. A.; Machon, D.; Pailhès, S.; Willand, A.; Caliste, D.; Botti, S.; San Miguel, A.; Goedecker, S.; Marques, M. A. L. Crystal Structure of Cold Compressed Graphite, *Phys. Rev. Lett.*, **2012**, 108, 065501.

(45) Amsler, M.; Botti, S.; Marques., M. A. L.; Lenosky, T. J.; Goedecker, S. Low-Density Silicon Allotropes for Photovoltaic Applications, *Phys. Rev. B*, **2015**, 92, 014101.

(46) Amsler, M.; Flores-Livas, J. A.; Huan, T. D.; Botti, S.; Marques, M. A. L.; Goedecker, S. Novel Structural Motifs in Low Energy Phases of $LiAlH_4$, *Phys. Rev. Lett.*, **2012**, 108, 205505.

(47) Flores-Livas, J. A.; Amsler, M.; Heil, C.; Sanna, A.; Boeri L.; Profeta, G.; Wolverton, C.; Goedecker, S.; Gross, E. K. U. Superconductivity in Metastable Phases of Phosphorus-Hydride Compounds under High Pressure, *Phys. Rev. B*, **2016**, 93, 020508.

(48) Roy, S.; Goedecker, S.; Hellmann, V. Bell-Evans-Polanyi Principle for Molecular Dynamics Trajectories and Its Implications for Global Optimization, *Phys. Rev. E*, **2008**, 77, 056707.

(49) Sicher, M.; Mohr, S.; Goedecker, S. Efficient Moves for Global Geometry Optimization Methods and Their Application to Binary Systems, *J. Chem. Phys.*, **2011**, 134, 044106-044106.

(50) Blöchl, P. E. Projector Augmented-Wave Method, *Phys. Rev. B*, **1994**, 50, 17953.

(51) Kresse, G. Ab Initio Molecular Dynamics for Liquid Metals, *J. Non-Cryst. Solids* **1995**, 192 , 222.

(52) Kresse, G.; Furthmüller, J. Efficiency of Ab-Initio Total Energy Calculations for Metals and Semiconductors Using a Plane-Wave Basis Set, *Comput. Mater. Sci.*, **1996**, 6, 15.

(53) Kresse, G.; Joubert, D. From Ultrasoft Pseudopotentials to the Projector Augmented-Wave Method, *Phys. Rev. B*, **1999**, 59, 1758.

(54) Perdew, J. P.; Burke, K.; Ernzerhof, M. Generalized Gradient Approximation Made Simple, *Phys. Rev. Lett.*, **1996**, 77, 3865.

(55) Togo, A.; Oba, F.; Tanaka, I. First-Principles Calculations of the Ferroelastic Transition between Rutile-Type and $CaCl_2$-Type SiO_2 at High Pressures, *Phys. Rev. B*, **2008**, 78, 134106.

(56) Giannozzi, P.; Baroni, S.; Bonini, N.; Calandra, M.; Car, R.; Cavazzoni, C.; Ceresoli, D.; Chiarotti, G. L.; Cococcioni, M.; Dabo, I.; Corso, A. D.; de Gironcoli, S.; Fabris, S.; Fratesi, G.; Gebauer, R.; Gerstmann, U.; Gougoussis, C.; Kokalj, A.; Lazzeri, M.; Martin-Samos, L.; Marzari, N.; Mauri, F.; Mazzarello, R.; Paolini, S.; Pasquarello, A.; Paulatto, L.; Sbraccia, C.; Scandolo, S.; Sclauzero, G.; Seitsonen, A. P.; Smogunov, A.; Umari, P.; Wentzcovitch, R. M. QUANTUM ESPRESSO: A Modular and Open-Source Software Project for Quantum Simulations of Materials, *Journal of Physics: Condensed Matter*, **2009**, 21, 395502.

(57) Allen P. B.; Dynes, R. C. Transition Temperature of Strong-Coupled Superconductors Reanalyzed, *Phys. Rev. B*, **1975**, 12, 905.

SYNOPSIS TOC. Creating new intermetallic compounds.